



Original Research

3D plotting in the preparation of newberyite, struvite, and brushite porous scaffolds: using magnesium oxide as a starting material

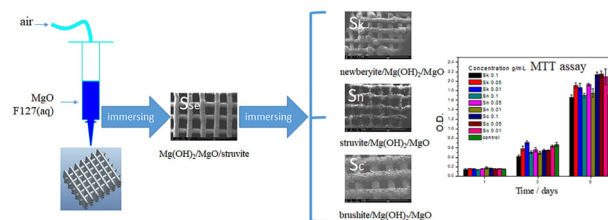
Xiaofeng Cao¹ · Haojun Lu² · Junli Liu¹ · Weipeng Lu¹ · Lin Guo¹ · Ming Ma¹ · Bing Zhang¹ · Yanchuan Guo^{1,2,3}

Received: 15 March 2019 / Accepted: 8 July 2019 / Published online: 19 July 2019
© Springer Science+Business Media, LLC, part of Springer Nature 2019

Abstract

Calcium phosphate (CaP)-containing materials, such as hydroxyapatite and brushite, are well studied bone grafting materials owing to their similar chemical compositions to the mineral phase of natural bone and kidney calculi. In recent studies, magnesium phosphate (MgP)-containing compounds, such as newberyite and struvite, have shown promise as alternatives to CaP. However, the different ways in degradation and release of Mg^{2+} and Ca^{2+} ions in vitro may affect the biocompatibility of CaP and MgP-containing compounds. In the present paper, newberyite, struvite, and brushite 3D porous structures were constructed by 3D-plotting combining with a two-step cementation process, using magnesium oxide (MgO) as a starting material. Briefly, 3D porous green bodies fabricated by 3D-plotting were soaked in $(NH_4)_2HPO_4$ solution to form semi-manufactured 3D porous structures. These structures were then soaked in different phosphate solutions to translate the structures into newberyite, struvite, and brushite porous scaffolds. Powder X-ray diffraction (XRD), scanning electron microscopy (SEM), and energy dispersive spectrometry (EDS) were used to characterize the phases, morphologies, and compositions of the 3D porous scaffolds. The porosity, compressive strength, in vitro degradation and cytotoxicity on MC3T3-E1 osteoblast cells were assessed as well. The results showed that extracts obtained from immersing scaffolds in alpha-modified essential media induced minimal cytotoxicity and the cells could be attached merely onto newberyite and brushite scaffolds. Newberyite and brushite scaffolds produced through our 3D-plotting and two-step cementation process showed the sustained in vitro degradation and excellent biocompatibility, which could be used as scaffolds for the bone tissue engineering.

Graphical Abstract



1 Introduction

In recent years, there has been an increase in injuries and diseases associated with bone defects. Thus, there has been urgent demand for natural and artificial synthetic bone

Supplementary information The online version of this article (<https://doi.org/10.1007/s10856-019-6290-2>) contains supplementary material, which is available to authorized users.

✉ Yanchuan Guo
yanchuanguo@mail.ipc.ac.cn

¹ Key Laboratory of Photochemical Conversion and Optoelectronic Material, Technical Institute of Physics and Chemistry, Chinese Academy of Sciences, 100190 Beijing, PR China

² Hangzhou Branch of Technical Institute of Physics and Chemistry, Chinese Academy of Sciences, Zhejiang, 310018 Hangzhou, PR China

³ University of Chinese Academy of Sciences, 100049 Beijing, PR China

grafts in clinical surgery [1, 2]. Artificial synthetic bone grafts are considered an alternative to autologous and allogeneic bone grafts owing to the refined components and structures, unlimited supply, and scarcely any immune rejection [3, 4]. 3D printing technologies are state-of-the-art manufacturing methods for fabricating patient-customized scaffolds for sites of bone grafting [5–8]. 3D-plotting, otherwise referred to as direct ink writing, is an extrusion-based, layer-by-layer method of fabrication performed at room temperature [6, 9–11]. Combined with a cementation process, bone grafting scaffolds can be prepared through 3D-plotting without the requirement for high-temperature sintering, which facilitates the incorporation of thermosensitive reagents, such as drugs, proteins, and cells [9, 10].

Calcium phosphate (CaP)-containing materials, such as hydroxyapatite and brushite, have been well studied and served as excellent bone repair materials [6, 12–14]. Magnesium phosphate (MgP)-based materials, such as struvite and newberyite, are also hard tissue materials that resemble those found in human kidney stones [15]. Studies including the MgP-containing materials have been concentrated on developing self-setting MgP cements. The field about MgP bone cement is relatively new compared with that of CaP, initiated to overcome the disadvantages of CaP cements, such as its low strength, slow setting time, and poor biodegradability [16]. Studies have demonstrated that MgP bone cements are safe for several applications and have better degradability than CaP bone cement [17–19]. Gburcek's group implanted struvite cement, brushite cement, and calcium deficient hydroxyapatite (CDHA) cement into the femoral condyle of adult merino sheep and the struvite cement had higher porosity and degradability than the CaP cements after 10 months [18]. They also evaluated the degradation rate of the struvite cement and CDHA cement and the new bone growth after their implant into trabecular bone of adult merino sheep [19]. The results showed that the struvite cement was almost completely degraded after 10 months and CDHA cement hardly degraded. In addition the MgP cement resulted in more new bone growth than the CDHA cement. The ceramic MgP family has numerous phases, such as the struvite, struvite-K, schertelite, newberyite, cattite, bobierrite, and farringtonite [16]. These ceramic MgP phases have different crystal structures, which endows the materials with different physicochemical and biological properties [15, 16].

Up to now, enormous effort has been made to fabricate the CaP and MgP 3D porous scaffolds via 3D-plotting method [20–27]. CaP-based bone implants and scaffolds were first prepared by Lewis' group via 3D-plotting [20]. Since then, various CaP-based materials, including hydroxyapatite, alpha-tricalcium phosphate (TCP), beta-TCP, and composites of HAp and beta-TCP, have been manufactured into scaffolds using 3D-plotting [21–23]. More recently,

Yun's and Park's groups have employed 3D-plotting combined with cementation chemistry to prepare struvite 3D scaffolds, using self-made farringtonite ($\text{Mg}_3(\text{PO}_4)_2$) powder that was prepared via high-temperature calcination as the reactant [24–27]. This method, however, needs a crushing treatment process to obtain a suitable particle size to meet the extrusion requirements. There is few other reports on MgP phases during the final hardening process.

In this paper, we report the preparation of newberyite ($\text{MgHPO}_4 \cdot 3\text{H}_2\text{O}$), struvite ($\text{MgNH}_4\text{PO}_4 \cdot 6\text{H}_2\text{O}$), and brushite ($\text{CaHPO}_4 \cdot 2\text{H}_2\text{O}$) 3D porous structures via facile 3D-plotting combined with a two-step cementation process incorporating phosphates through solution immersion. Similar to most MgP cement formulations, magnesium oxide (MgO) was selected as the starting material, and used without high-temperature calcination. The fabricated 3D porous green bodies were immersed in different phosphate aqueous solutions for transformation into MgP- or CaP-based 3D porous scaffolds. Properties, such as porosity, compressive strength, in vitro degradation, and cytotoxicity, were studied in detail.

2 Experimental section

2.1 Fabrication of the scaffolds

All reagents were used without further purification. The fabrication of the porous scaffolds was performed with a homemade 3D-plotting device equipped with a gas-pushed device and a three-axis positioning system. Light MgO was employed as the raw material and 0.15 g/mL pluronic F127 aqueous solution was used as the binder. In a typical fabrication procedure, F127 (3 mL) was introduced into MgO powder (4 g, AR) with manual continuous stirring to form an injectable paste as the ink. The paste was loaded into a syringe that was fitted with a 0.3-mm diameter cylindrical nozzle. The dosing pressure to the syringe was 0.2–0.4 MPa and the speed of the positioning system was 30 mm/s. The fabricated MgO porous green bodies were dried at room temperature overnight. Green bodies were then soaked in phosphate aqueous solution using a two-step procedure. First, the green bodies were immersed in 0.5 mol/L of $(\text{NH}_4)_2\text{HPO}_4$ solution for 3 days. The obtained semi-manufactured scaffolds (hereafter, “S_{se} scaffolds”) were washed with deionized water several times and then immersed in KH_2PO_4 (1 mol/L), $\text{NH}_4\text{H}_2\text{PO}_4$ (2 mol/L), and $\text{Ca}(\text{H}_2\text{PO}_4)_2$ (saturated solution dissolved with H_3PO_4 1.46 mol/L) phosphate aqueous solutions for 3 d, respectively. The resultant scaffolds are designated as S_k, S_n, and S_c, respectively. The phosphate aqueous solutions were kept fresh via displacement everyday in the period. The complete soaking cementation process was performed at room

temperature. Finally, the scaffolds were washed with deionized water several times and then dried in air at 60 °C for 24 h.

2.2 Characterization of the scaffolds

The phases of the scaffolds were characterized by X-ray powder diffraction (XRD) on a powder X-ray diffractometer (Bruker, D8, Germany) with Cu K α radiation ($\lambda = 1.5406 \text{ \AA}$) and recorded in the 2θ range of 10–70°. Scanning electron microscopy (SEM) and energy dispersive spectrometry (EDS) were measured on a scanning electron microanalyzer (Quanta, FEG 250, USA) with an operating voltage of 10 or 15 kV.

2.3 Porosity measurement

The porosity measurement method used in this study was performed as described elsewhere [28]. Porosity of the MgP and CaP scaffolds (10 × 10 × 8 mm) was measured in a specific gravity bottle using ethanol immersion based on Archimedes' principle. First, scaffolds were dried at 100 °C for 24 h and weighed, and the results recorded as W_s . Next, the bottle was filled with ethanol, weighed, and recorded as W_1 . The scaffold was immersed in the bottle filled with ethanol and weighed, with the results recorded as W_2 . Finally, the ethanol-saturated scaffold was taken out from the bottle, and the final weight of the bottle and ethanol was measured as W_3 . Porosity was calculated as following equation:

$$\text{Porosity (\%)} = [(W_2 - W_3 - W_s)/\rho_e]/[(W_1 - W_3)/\rho_e] \times 100\%,$$

where $(W_1 - W_3)/\rho_e$ is the total volume of the scaffold, including the pores, and $(W_2 - W_3 - W_s)/\rho_e$ is the pore volume in the scaffold. Six specimens were tested for each scaffold.

2.4 Mechanical properties

Compressive strength tests were performed in a universal mechanical testing machine (Instron 5960, USA) equipped with a load cell of 20 kN, at a cross-head speed of 0.5 mm/min, until the scaffolds were fractured. The loading direction was perpendicular to the layer-by-layer deposition planes of the scaffolds. Six specimens were tested for each scaffold (10 × 10 × 8 mm).

2.5 Degradation in vitro

To measure scaffold degradation in vitro, scaffolds were soaked in PBS solution (pH 7.4) in plastic centrifuge tubes with the volume to mass ratio of 200 mL/g in a bath shaker at constant temperature (37 °C) and 60 r/min for 1, 2, 3, and 4 weeks. At the end of each period, the PBS solution was

refreshed and the weight loss was calculated based on the following equation:

$$\text{Weight loss (\%)} = (W_0 - W_t)/W_0 \times 100\%,$$

where W_0 is the weight of the dried scaffold before degradation and W_t is the weight of the scaffold at the set time point. The pH of the PBS solution was measured and recorded at each time point during the degradation process. Four specimens were tested for each scaffold (10 × 10 × 2 mm).

2.6 In vitro cytotoxicity assay

Cytotoxicity assays using methyl thiazolyl tetrazolium (MTT) were conducted on MC3T3-E1 osteoblast cells (Chinese Academy of Medical Sciences) exposed to extracts of the scaffolds. Scaffolds (10 × 10 × 8 mm) were sterilized by epoxyethane and then placed in tightly capped sterilized centrifuge tubes containing alpha-modified essential media (alpha-MEM) solution at 37 °C for 3 days. The extracts were collected and filtered through a 200-nm microporous membrane for sterilization and to remove small particles. The extracts were then mixed with a final concentration of 10% fetal bovine serum (FBS). The final ratio between the scaffold and the extraction medium was 0.1 g/mL. Extracts were diluted with alpha-MEM supplemented with 10% FBS to 0.1, 0.05, and 0.01 g/mL for tests. MC3T3-E1 osteoblast cells were seeded into 96-well plates at a density of 500 cells per well and grew for 24 h in alpha-MEM supplemented with 10% FBS. Six wells per treatment were prepared. After 24 h, non-attached cells were removed and the media was replaced with 200 μ L media containing extracts at various concentrations. Cells were cultured for 1, 3, and 5 days, respectively, with the media refreshed every 2 days. Alpha-MEM supplemented with 10% FBS was used as a blank control.

MTT cell viability assay was used to evaluate the cytotoxicity. MTT reagent (20 μ L, 5 mg/mL) was added to each well and incubated for 4 h. Medium was then carefully removed and 150 μ L of dimethyl sulfoxide was added to each well and pipetting up and down several times. The 96-well plates were incubated on a rocker shaker for 10 min at room temperature, and the absorbance was then measured at 490 nm on a microplate reader. In previous reports [29, 30], free Mg²⁺ can lead to false positive or negative results in an MTT assay. Therefore, the reported values were normalized to the background levels for each material. In our study, there were negligible effects from the Mg²⁺ ions.

2.7 SEM and microscope analysis

MC3T3-E1 osteoblast cells were seeded at a density of 50,000 cells onto 10 × 10 × 2 mm S_k, S_n, and S_c scaffolds

housed in 24-well plates, using glass as the control. The morphology changes of MC3T3-E1 osteoblast cells after 3 days in standard culturing conditions were observed by SEM. Cell/scaffold samples were washed thrice with PBS, and fixed with 2.5% glutaraldehyde solution at 4 °C for 4 h. Cells were then dehydrated in a series of graded ethanol solutions (30, 50, 70, 90, 95 and 100 % v/v) for 5 min and dried in vacuum at 50 °C for 72 h. Finally, the samples were sputtered with Au for SEM observation. The cells growth on the glass surface and bottom of the 24-well plates in the case of cell/scaffold samples were observed on an inverted microscope.

2.8 Statistical analysis

Statistical analysis was carried out using one-way ANOVA analysis, followed by Tukey post hoc tests to determine the significance. Values are expressed as the mean \pm standard deviation. Statistical analysis was performed with SPSS v22 (Chicago, IL, USA). Statistical significance was set at $P < 0.05$.

3 Results

3.1 Phases and morphologies of the scaffolds

Figure 1a shows the XRD pattern of the S_{se} semi-manufactured 3D porous scaffolds before the second immersion step. The major diffraction peaks can be indexed to the hexagonal phase of $Mg(OH)_2$ (JCPDS card No. 07-0239) and the cubic phase of MgO (JCPDS card No. 89-4248). The other weak diffraction peaks at 20.76°, 30.54°, and 32.86° can be indexed to the orthorhombic phase of

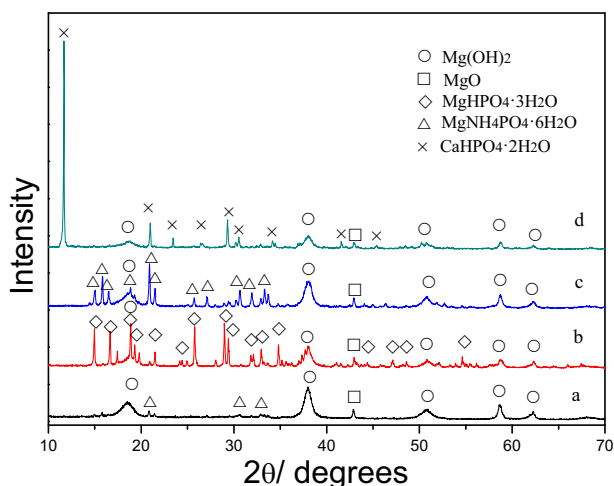


Fig. 1 Powder X-ray diffraction (XRD) patterns of the **a** S_{se} ($Mg(OH)_2/MgO/MgNH_4PO_4 \cdot 6H_2O$), **b** S_k ($MgHPO_4 \cdot 3H_2O$), **c** S_n ($MgNH_4PO_4 \cdot 6H_2O$), and **d** S_c ($CaHPO_4 \cdot 2H_2O$) scaffolds

$MgNH_4PO_4 \cdot 6H_2O$ (JCPDS card No. 71-2089). The S_{se} was then soaked in various phosphates aqueous solutions to obtain fresh porous structures (Fig. 1b–d). The newberyite, struvite, and brushite phases are identified by comparison with data from JCPDS card No. 72-0023 (the orthorhombic phase of $MgHPO_4 \cdot 3H_2O$), No. 71-2089 (the orthorhombic phase of $MgNH_4PO_4 \cdot 6H_2O$), and No. 72-0713 (the monoclinic phase of $CaHPO_4 \cdot 2H_2O$). The other diffraction peaks are ascribed to the $Mg(OH)_2$ intermediate formed in the first step cementation process and the unreacted raw MgO . Specially, the (020) diffraction peak at 11.70° for the brushite phase has the extremely strong intensity, which indicates the preferred oriented growth of the {020} crystallographic plane [31].

Figure 2 shows the SEM images of the 3D porous structures and physical parameters of the strut diameters and pore sizes are summarized in Table 1. The deviation in strut diameters and pore sizes may be due to the shake during the 3D-plotting operation. Some smaller pores (10–100 μm) can be seen on the struts of the S_{se} scaffolds and the surface of the S_{se} scaffold comprises a collection of irregular polyhedrons in the range of $\sim 1 \mu m$ to several micrometers

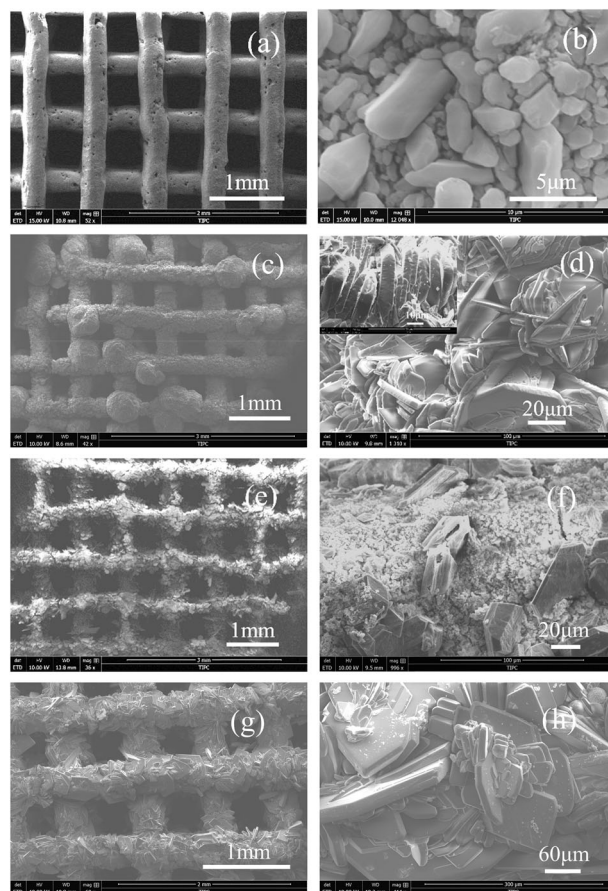
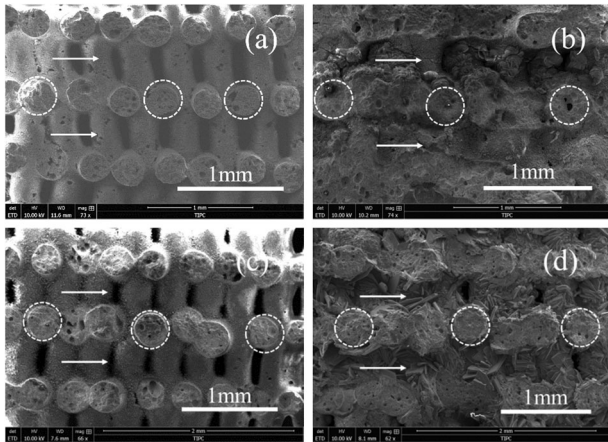


Fig. 2 Scanning electron microscopy (SEM) images of **a, b** S_{se} ($(OH)_2/MgO/MgNH_4PO_4 \cdot 6H_2O$), **c, d** S_k ($MgHPO_4 \cdot 3H_2O$), **e, f** S_n ($MgNH_4PO_4 \cdot 6H_2O$), and **g, h** S_c ($CaHPO_4 \cdot 2H_2O$) scaffolds

Table 1 Scaffold characteristics and dimensions

Scaffold	S_{se}	S_k	S_n	S_c
Strut diameter (mm)	0.27–0.39	0.33–0.39	0.31–0.49	0.38–0.49
Pore size (mm)	0.39–0.59	0.35–0.46	0.36–0.64	0.31–0.45

S_{se} : $Mg(OH)_2/MgO/MgNH_4PO_4 \cdot 6H_2O$; S_k : $MgHPO_4 \cdot 3H_2O$; S_n : $MgNH_4PO_4 \cdot 6H_2O$; S_c : $CaHPO_4 \cdot 2H_2O$

**Fig. 3** SEM images of the internal structures of the **a** S_{se} ($Mg(OH)_2/MgO/MgNH_4PO_4 \cdot 6H_2O$), **b** S_k ($MgHPO_4 \cdot 3H_2O$), **c** S_n ($MgNH_4PO_4 \cdot 6H_2O$), and **d** S_c ($CaHPO_4 \cdot 2H_2O$) scaffolds

(Fig. 2a, b). After the second immersion step of the cementation process, the S_{se} scaffolds were transformed into the S_k , S_n , and S_c scaffolds, with which the macroscopic structures were maintained. To a certain extent, the strut diameters and pore sizes changed. The struts of S_k scaffolds are constructed by microscale plates in thickness of about 1.2–5.8 μm (Fig. 2d). Semi-spherical particles (~0.44–0.69 mm), that are formed by microplates in different thickness (3.39–8.91 μm), locate on the struts of the S_k scaffolds and cover some of the pores (Fig. 2c, d inset). The struts of S_n scaffolds are constructed by sub-microscale and microscale polyhedron particles (Fig. 2e, f), while the struts of the S_c scaffolds (Fig. 2g, h) are constructed by microplates in thickness of about 10–20 μm .

Figure 3 shows the SEM images of the down-up internal pore tunnel structure and cross-sections of strut in the four scaffolds, as marked by arrows and circles, respectively. The down-up interconnected pore tunnels (arrows) are visible in all of the scaffolds. The struts of the S_{se} and S_n scaffold (marked by circles) exhibit a clear circular profile (Fig. 3a, c). For the S_k and S_c scaffolds, semi-spherical particles and microplate particles are found within the internal pore tunnels and these particles partly fill the interlayer pores, respectively (Fig. 3b, d).

Elemental mapping was used to visualize the distribution of the elements in the cementation process. Figure 4 shows

the strut morphologies and elemental mappings of the four scaffolds. In the S_{se} , S_k , and S_n scaffolds, the element Mg distributes inside and outside of the struts (Fig. 4b, e, h); however, in the S_c scaffolds, there is no obvious Mg signal detectable outside the struts (Fig. 4k). The P signals are found mainly at the edges of the struts (Fig. 4c, f, i, l). These results indicate that the phosphate solutions react with the raw materials in the solid-liquid interfaces and the freshly formed phases coating on the surface of the struts hinder the reaction at a greater depth. However, a small amount of element P is still found within the inner of the struts (Fig. 4c, f, i, l). In the S_c scaffolds, a high signal intensity of the element Ca is detected outside the struts (Fig. 4m), which is coincident with the P signal (Fig. 4l).

Surface elemental mapping of the internal structures of the scaffolds were also measured. On the strut surface of the S_{se} (Fig. S1 in supporting information (SI)), S_k (Fig. S2 in SI) and S_n (Fig. S3 in SI), Mg, P, and O signals were detected and shown to overlap with each other. On the strut surface of the S_c scaffold, Ca, P, and O signals overlapped, with rather weak but detectable Mg signal detected (Fig. S4 in SI). Combined with the XRD pattern (Fig. 1), the phases of the strut surface can be ascribed to the formation of brushite, with little amount of MgP phase.

3.2 Porosity and mechanical properties of the MgP and CaP scaffolds

Figure 5 shows the porosity of the four scaffolds. S_{se} has the highest porosity ($57.5 \pm 3.36\%$) compared with the scaffolds subjected to the second immersion step, and all the samples show a decrease in porosity (S_k , S_n , and S_c scaffolds had porosity values of $39 \pm 2.37\%$, $55.3 \pm 4.69\%$, and $25.8 \pm 3.96\%$, respectively). Although there is no significant difference between S_{se} and S_n ($P > 0.05$), S_c has obviously lower porosity than that of the others ($P < 0.05$). It is necessary to point out that the porosity values are higher than the original porosity from the printed samples, which can be attributed to the evaporation of crystalline water in MgP and CaP phases under the thermotreatment of the sample to 100 °C. This leads to the change of phase composition and density.

Figure 6 shows the compressive strengths of the four scaffolds. S_{se} scaffolds has the lowest compressive strength (2.4 ± 0.39 MPa), which can be easily crumbled by hand. However, after the second step of the cementation process, the compressive strengths of S_k , S_n , and S_c scaffolds obviously increase to 6.1 ± 0.36 , 6.6 ± 1.2 , and 11.2 ± 2.6 MPa, respectively, in which S_c has a significantly higher compressive strength compared with the others ($P < 0.05$). The compressive strength of the MgP and CaP scaffolds matches that of human cancellous bone [1].

Fig. 4 Cross-sectional morphologies and elemental mappings of the S_{se} , S_k , S_n , and S_c scaffolds. **a–c** S_{se} ($Mg(OH)_2/MgO/MgNH_4PO_4 \cdot 6H_2O$) scaffolds: **a** SEM image, **b** Mg, and **c** P. **d–f** S_k ($MgHPO_4 \cdot 3H_2O$) scaffolds: **d** SEM image, **e** Mg, and **f** P. **g–i** S_n ($MgNH_4PO_4 \cdot 6H_2O$) scaffolds: **g** SEM image, **h** Mg, and **i** P. **j–m** S_c ($CaHPO_4 \cdot 2H_2O$) scaffolds: **j** SEM image, **k** Mg, **l** P, and **m** Ca

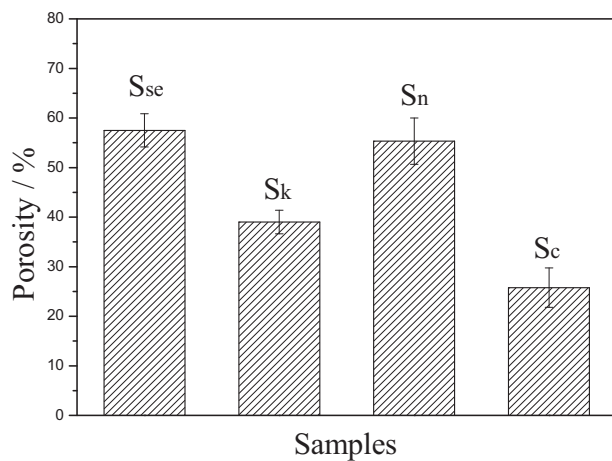
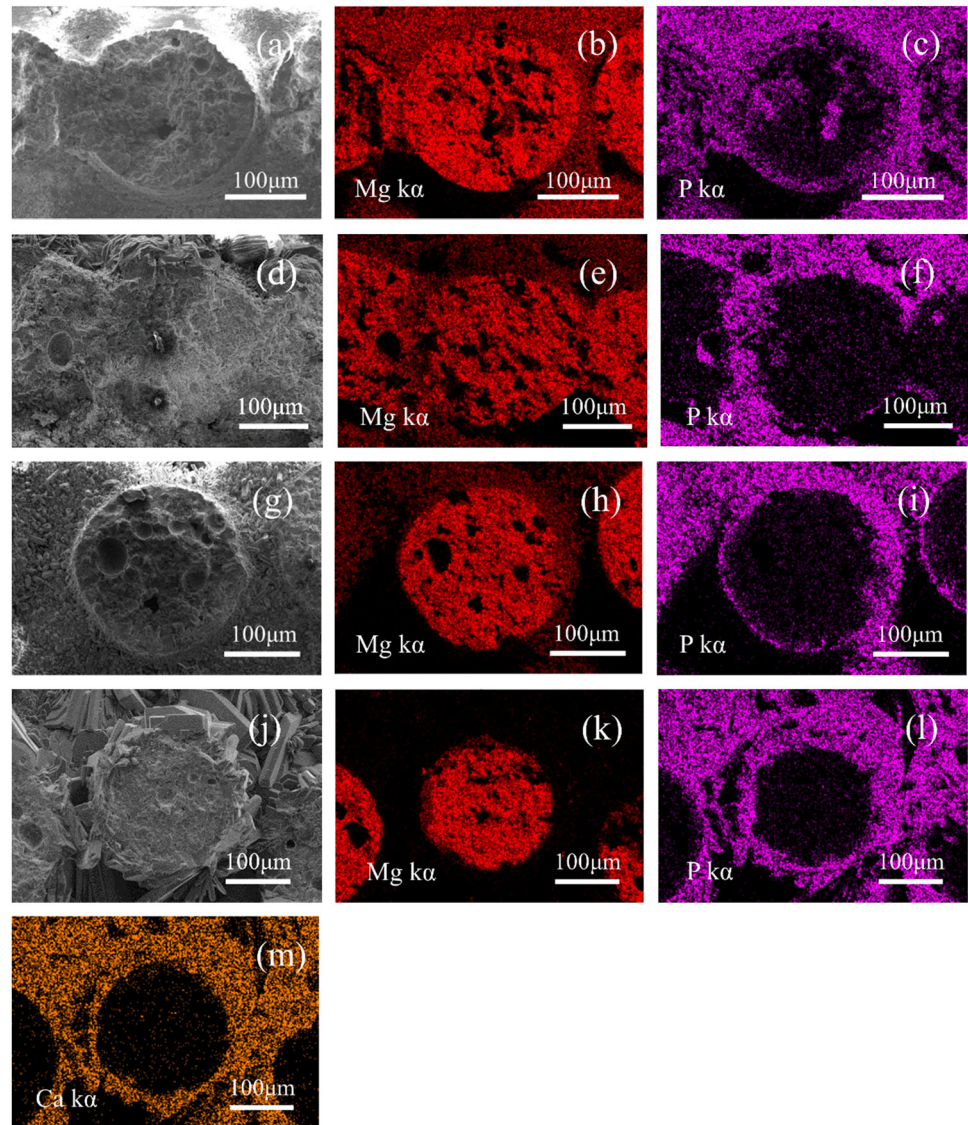


Fig. 5 Porosity of the S_{se} ($Mg(OH)_2/MgO/MgNH_4PO_4 \cdot 6H_2O$), S_k ($MgHPO_4 \cdot 3H_2O$), S_n ($MgNH_4PO_4 \cdot 6H_2O$), and S_c ($CaHPO_4 \cdot 2H_2O$) scaffolds

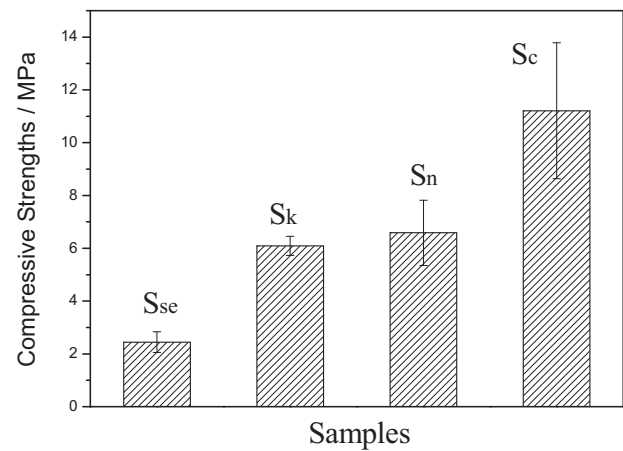


Fig. 6 Compressive strength of the S_{se} ($Mg(OH)_2/MgO/MgNH_4PO_4 \cdot 6H_2O$), S_k ($MgHPO_4 \cdot 3H_2O$), S_n ($MgNH_4PO_4 \cdot 6H_2O$), and S_c ($CaHPO_4 \cdot 2H_2O$) scaffolds

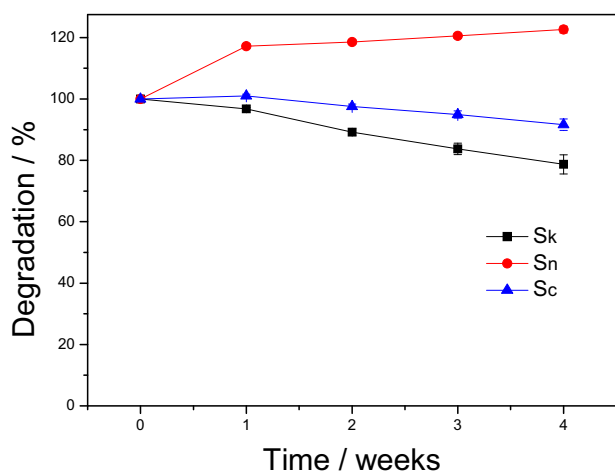


Fig. 7 In vitro degradation of the S_k (MgHPO₄·3H₂O), S_n (MgNH₄PO₄·6H₂O), and S_c (CaHPO₄·2H₂O) scaffolds in PBS at 37 °C for the indicated setting times

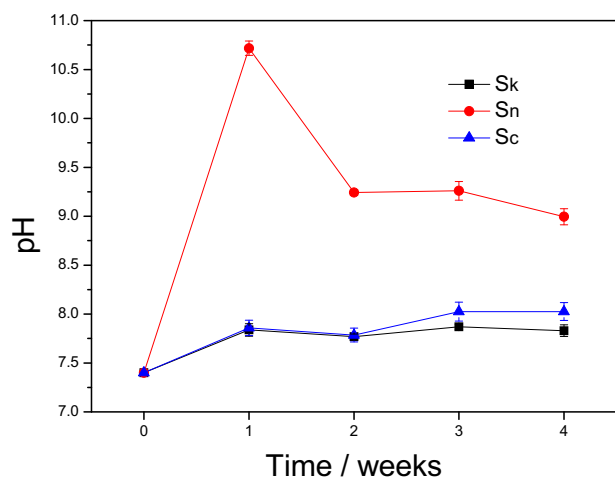


Fig. 8 Changes in the pH of PBS during in vitro degradation of the S_k (MgHPO₄·3H₂O), S_n (MgNH₄PO₄·6H₂O), and S_c (CaHPO₄·2H₂O) scaffolds

3.3 In vitro degradation and pH values of PBS

Figure 7 shows the in vitro degradation ratios of the scaffolds in PBS after 7, 14, 21, and 28 days at 37 °C. The S_k scaffolds degrade gradually over time, with a weight loss ratio of ~22% over 28 days. The weight ratio of the S_c scaffolds increase slightly to 101 ± 0.54% at 7 d, and then decrease gradually to 91.6 ± 1.86% by 28 days. The weight ratio of the S_n scaffolds increase rapidly to 117.2 ± 0.78% at 7 days, and maintains at slightly higher levels of 122.6 ± 1.1% until 28 days.

The pH of the PBS solutions was measured at each time point. As shown in Fig. 8, an alteration in the pH of PBS from 7.4 to 7.83 (S_k), 9.0 (S_n), and 8.03 (S_c), respectively, induced by S_k, S_n and S_c occurs after 28 days. Although

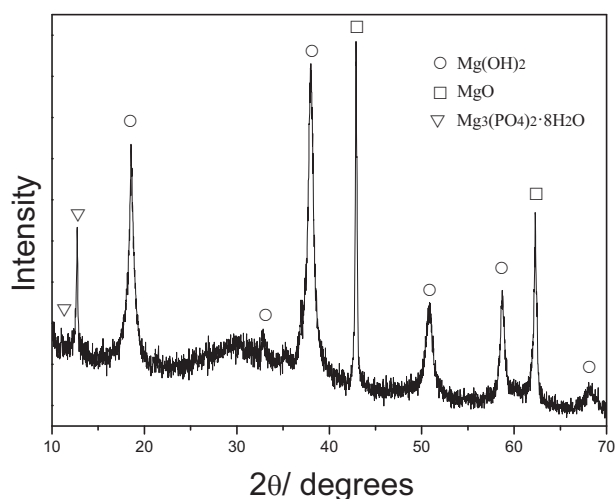


Fig. 9 Powder X-ray diffraction (XRD) pattern of the S_n (MgNH₄PO₄·6H₂O) degraded in PBS for 28 days

slightly alkaline environments were obtained during the degradation of S_k and S_c, degradation of the S_n led to a much bigger change in the pH, with pH = 10.7 achieved after 7 days, and a pH of about 9 maintained for the remainder of the tests.

The phase change of the S_n scaffold were studied because it showed the abnormal weight increase during in vitro degradation process. Figure 9 shows the XRD pattern of the S_n scaffolds soaked in PBS solution after 28 days. The struvite phase disappeared and new MgP phases were formed. Comparing with data from JCPDS card No. 16-0330, the diffraction peaks at 11° and 12.72° can be indexed to the monoclinic phase of Mg₃(PO₄)₂·8H₂O. A weak and wide diffraction peak around 30° can be ascribed to the MgP amorphous phase [30, 32]. In addition, Mg(OH)₂ and the unreacted raw MgO exist in the S_n scaffolds.

3.4 In vitro cytotoxicity assay

The MTT assay was used to evaluate the cytotoxicity of the extracts obtained from scaffolds immersed in alpha-MEM for 3 days. As shown in Fig. 10, MC3T3-E1 osteoblast cells show good viability in extracts of S_k, S_n, and S_c scaffolds at various concentrations for 1, 3, and 5 days compared with the blank control group.

Figure 11 shows SEM images of MC3T3-E1 osteoblast cells attachment on glass, S_k, S_n, and S_c scaffolds. MC3T3-E1 osteoblast cells attach and spread well on the glass, S_k and S_c scaffold surface. However, almost no cells can be observed on the surface of the S_n scaffolds.

Inverted microscope images (Fig. S6a, b, and d in SI) shows that MC3T3-E1 osteoblast cells grow well on glass surface and bottom of 24-well plates in the case of

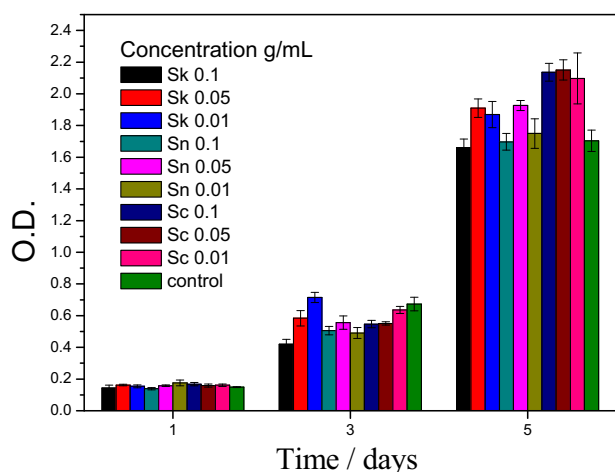


Fig. 10 MC3T3-E1 osteoblast cells exposed to extracts of the S_k ($MgHPO_4 \cdot 3H_2O$), S_n ($MgNH_4PO_4 \cdot 6H_2O$), and S_c ($CaHPO_4 \cdot 2H_2O$) scaffolds at different concentrations for 1, 3 and 5 days

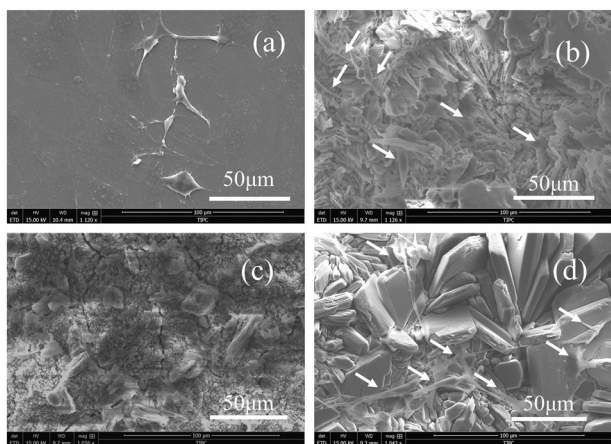


Fig. 11 SEM images showing the attachment and survival of the MC3T3-E1 osteoblast cells cultured on **a** glass (as control), **b** S_k ($MgHPO_4 \cdot 3H_2O$), **c** S_n ($MgNH_4PO_4 \cdot 6H_2O$), and **d** S_c ($CaHPO_4 \cdot 2H_2O$) scaffold surfaces for 3 days

newberyite and brushite. Contrarily the dead MC3T3-E1 cells are observed, which the cells became circular in the case of struvite (Fig. S6c in SI). The SEM and inverted microscope images indicate that the newberyite and brushite scaffolds can support the cells and the struvite scaffold cause cytotoxicity.

4 Discussion

In this paper, we report the preparation of newberyite, struvite, and brushite 3D porous scaffolds via a facile 3D-plotting process, employing the light MgO and F127 solution as the raw materials. In most biomedical applications using MgP cement formulations, MgO is used as the starting material [16]. However, MgO was not

Table 2 pH values of the phosphate aqueous solutions used in the cementation process

Solution	$(NH_4)_2HPO_4$	KH_2PO_4	$NH_4H_2PO_4$	$Ca(H_2PO_4)_2$
pH value	7.91	4.05	3.76	2.32

thermotreated at high-temperature in the present paper. Thus the calcination and crush process were avoided, which could maintain the high chemical activity of the light MgO and achieve a rapid hardness of the material. F127 has good biocompatibility and has been approved by the US FDA as a food additive or in pharmaceuticals [33–35]. Light MgO was dispersed into the F127 solution to create an injectable paste ink, from which three goals could be achieved: (1) the paste ink could be extruded fluently because of the small size of the MgO and the excellent rheological properties of the F127 solution [36]; (2) the struts extruded from the cylindrical nozzle had sufficient mechanical strength so that the subsequent stacking process could be conducted continuously, and (3) the green bodies before hardening had sufficient washout resistance to maintain a 3D porous structure when they were immersed into the $(NH_4)_2HPO_4$ solution (0.5 mol/L) for preliminary hardening.

After preliminary hardening, the resultant S_{se} scaffold was immersed into various phosphate aqueous solutions to obtain the final 3D porous scaffolds. The profiles and down-up interconnected pore tunnels were maintained in all of the scaffolds (Figs 2 and 3). During this second step, green bodies may dissolve or disintegrate. Loss of 3D structure can be ascribed to the acidity of the phosphate aqueous solutions (Table 2). Indeed, we noted the formation of a small amount of $MgNH_4PO_4 \cdot 6H_2O$ on the surface of the struts after the preliminary hardening (Figs 1 and 4b, c), and this formation could retard the scaffolds from corrosion in the acid phosphate aqueous solutions. Yet, the solution used in the preliminary hardening stage was slightly alkaline and MgO did not react well. Most of the MgO disappeared by hydrolysis to yield $Mg(OH)_2$ that formed the main phase of the S_{se} scaffold and a small amount of $MgNH_4PO_4 \cdot 6H_2O$ formed on the surface of the struts (Figs 1 and 4b, c). In most MgP cement formulations prepared from MgO and potassium phosphate salts, the final hardening product is struvite-K in general [37–39]. In the present study, however, the formed phase of the S_k scaffolds was newberyite rather than struvite-K when the S_{se} scaffolds were immersed in KH_2PO_4 solution (1 mol/L) (Fig. 1), due to the acidity of the KH_2PO_4 solution (Table 2). The Newberyite phase is stable in KH_2PO_4 solution with a starting pH of 4.05. Because the KH_2PO_4 solution was refreshed daily, the cementation process was conducted in a constantly acidic environment, and the newberyite could not further transform into struvite-K [40]. The main phase of S_n was struvite when the S_{se} scaffolds were immersed in $NH_4H_2PO_4$

solution (2 mol/L). Although the starting pH of $\text{NH}_4\text{H}_2\text{PO}_4$ solution is lower than that of the KH_2PO_4 solution (Table 1), struvite will dominate as a final structure across a wide range of pH values [41]. In addition, the solubility of struvite and newberyite will affect the final phase of the S_n [41]. The newly formed struvite and newberyite phases coated on the surface of the struts and had different microstructures (Figs 2c–f and 4d–i). Compared with the struvite scaffolds constructed by polyhedron particles with wide size distribution from submicron to tens of microns, the newberyite scaffolds was constructed by the microplates possessing more regular morphologies and bigger size (Fig. 2d, f). Based on the previous reports [42–46], the crystal growth of $\text{MgNH}_4\text{PO}_4 \cdot 6\text{H}_2\text{O}$ and $\text{MgHPO}_4 \cdot 3\text{H}_2\text{O}$ is complex and various factors such as pH, temperature, reactants, ion species and strength, and supersaturation can easily influence the crystal growth process. Hence, the reaction conditions should be controlled precisely.

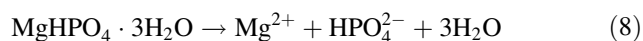
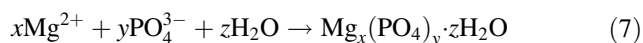
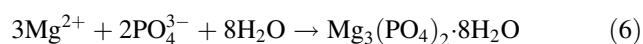
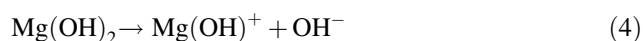
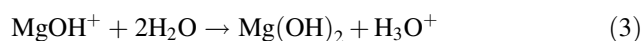
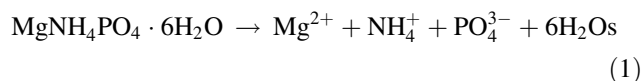
When the S_{se} scaffolds were immersed in $\text{Ca}(\text{H}_2\text{PO}_4)_2$ solution (saturated solution dissolved with H_3PO_4 1.46 mol/L), the main phase of S_c was brushite which was constructed by the microplates with the thickness of 10–20 μm (Fig. 2h). The size of the structural units was bigger than that of the S_k and S_n . The (020) diffraction peak at 11.70° in the XRD pattern (Fig. 1) exhibits the extremely high intensity and the diffraction peak intensity ratio of (020) to (12-1), (040), (14-1) or (121) are higher than that of the standard pattern in JCPDS card No. 72-0713 (the monoclinic phase of $\text{CaHPO}_4 \cdot 2\text{H}_2\text{O}$). This phenomenon usually corresponded to the plate-like structures, confirmed by the SEM images (Fig. 2g, h) [31]. The XRD pattern and the SEM images indicate the preferred oriented growth of the {020} crystallographic plane, in agreement with the previous report [31]. In order to investigate the transformation process from the primary products S_{se} to brushite, the time-depend experiments were performed. The S_{se} scaffolds were immersed in $\text{Ca}(\text{H}_2\text{PO}_4)_2$ solution for 10, 30 min, 1, 2 h, 1 and 2 days, respectively. As the immersing time prolonged, the diffraction peak intensity of brushite increased rapidly and the diffraction peak of $\text{Mg}(\text{OH})_2$ and MgO decreased gradually (Fig. S5 in SI). The MgP phases were undetectable during the whole reaction process, which indicated that little amount of MgP phases were produced (Fig. 1 and Fig. S5 in SI). It is reasonable that the newberyite and $\text{Mg}_3(\text{PO}_4)_2 \cdot n\text{H}_2\text{O}$ phases cannot form precipitates from the $\text{Ca}(\text{H}_2\text{PO}_4)_2$ solution with a starting pH of 2.32, while the brushite can easily crystallize and stably exist [15, 40, 47]. The Ca, P, and O elemental signals detected on the strut surface overlap with each other and the Mg elemental signal is almost negligible (Fig. S4 in SI). The content of element Mg is *ca.* 0.2 wt% on the strut surface according to the EDS results. The elemental mappings of the strut cross-section show that Mg mainly distributes inside of the struts where

the P signal is very weak (Fig. 4k, i). The results indicate that the element Mg mainly exists in the form of MgO and $\text{Mg}(\text{OH})_2$, which is in agreement with the XRD patterns (Fig. 1 and Fig. S5 in SI). It is noted that a particle with the size of *ca.* 10 μm marked by arrow occurs on the bottom of the SEM image (Fig. S4a in SI). Elemental mappings of the particle show that Mg and O signals are strong. Contrarily, Ca and P signals are weak. It is speculated that the main components of the particle is MgO or $\text{Mg}(\text{OH})_2$. The particle might drop from inside of the struts when the scaffolds were sliced, because MgO or $\text{Mg}(\text{OH})_2$ hardly appear on the strut surfaces after the second immersion step.

The morphologies, structures, and porosities of the scaffolds can be easily modified by adjusting the parameters of the 3D-plotting process. The large pore size and porosity are benefit for the bone ingrowth and vascularization in the bone repair process. However it is harmful to the mechanical properties of the scaffolds. Therefore the balance between microstructures and mechanical properties is highly required [10]. In this paper, the porosity of the scaffolds was fixed at 60%. The porosity of the S_{se} scaffolds was about 58%, which was very close to the fixing ratio. We show that the porosities of the scaffolds decrease after the second treatment stage (Fig. 5). The semi-spherical particles present on the S_k scaffold blocked the pores and decreased the final porosity of the material (Figs 2c and 5). However, these semi-spherical particles interrupted the struts, and thereby reduced the compressive strength of the S_k scaffolds (Fig. 6). In comparison, S_c scaffolds exhibited higher compressive strength but lower porosity due to the increase in strut diameter and the slight decrease in the pores size (Figs 5, 6 and Table 1). Compressive strength is also affected by the nature of components and microstructures of the scaffolds. Compared with the S_{se} scaffolds, the S_n scaffolds had higher compressive strength although they possessed the almost identical porosity. The higher mechanical properties of the S_n scaffolds could be attributed to the more struvite phase coated on the struts surface and interlocking microstructure formed in the hardening and stiffening process [48]. However, the compressive strength of the S_k , S_n and S_c scaffolds matches that of human cancellous bone, which ranges from 2 to 12 MPa and depends on age and location within the body [1, 49].

The *in vitro* degradation rate is an important property of bone repair scaffolds. Usually, MgP cements have higher dissolution rates than CaP cements. However, there are variations in the solubility of different phases of MgP and CaP. The relative dissolution of cements typically follows struvite < brushite < newberyite [16], which is consistent with the results in our experiments. The S_k scaffolds degraded consistently in PBS over the 28 d. The weight ratios of the S_c scaffolds slightly increased at 7 days, then decreased consistently over the next 3 weeks. In contrast,

the weights of the S_n scaffolds increased consistently throughout the experiment, which was contrary to the previous reports [16–19]. The reason for the increased weight could be ascribed to the unreacted MgO and $Mg(OH)_2$ existing in the scaffolds (Figs 1 and 4g–i). When the scaffolds were soaked in PBS solution, partial struvite phase on the surface of scaffolds could degrade to form the Mg^{2+} , NH_4^+ , and PO_4^{3-} (Eq. 1) [41]. The inner MgO was exposed to PBS system and immediately reacted with H_2O to form $Mg(OH)_2$ (Eqs. 2, 3) [48]. Abundant H_2O promoted the dissolution of $Mg(OH)_2$ to release the Mg^{2+} and OH^- which induced the scaffold/PBS system to be alkaline (Eqs. 4, 5) [41, 48, 50]. Mestres reported that the aged-struvite-cement extracts prepared in PBS was alkaline and the pH was about 9.1 [51]. In the present research, the high pH of 10.7 at the first week was attributed to the reaction between MgO and H_2O . When the immersing time was prolonged, $Mg(OH)_2$ coating on the surface of the scaffolds prohibited the hydrolysis of MgO. As the PBS solution was refreshed every week, the pH value trended to be constant at *ca.* 9.0 which was very close to that in the previous report [51]. $Mg_3(PO_4)_2 \cdot 8H_2O$ and MgP amorphous phase were produced according to the XRD pattern of the scaffold soaked in PBS for 4 w (Fig. 9 and Eqs. 6, 7). The combination between the degradation of the $MgNH_4PO_4 \cdot 6H_2O$ and generation of $Mg(OH)_2$ and new MgP phases resulted in the scaffolds weight increase. As immersing time was prolonged, the degradation rate and generation rate reached a dynamic equilibrium and the weight hardly grew. On the other hand, when the newberyite and brushite scaffolds were immersed in the PBS, plenty of H^+ were released to neutralize the OH^- and the scaffold/PBS system maintained constant pH (Fig. 9 and Eqs. 8–10).



In the present study, the extracts of S_k , S_n , and S_c scaffolds all showed good cytocompatibility. However, when the cells were seeded onto the scaffolds directly, few cells were viable within 3 days on the S_n scaffolds and all of the cells died on the bottom of the 24-well plates (Fig. 11c and Fig. S6c in SI). This cytotoxicity may be attributed to the high pH of the S_n scaffolds when it degrades (Fig. 8). By comparison, the S_k and S_c scaffolds showed good cytocompatibility with adherent MC3T3-E1 osteoblast cells identified on the surfaces of the scaffolds and the cells on the bottom of 24-well plates grew well (Fig. 11b, d and Fig. S6b, d in SI).

5 Conclusion

In the present paper, 3D porous structures of newberyite ($MgHPO_4 \cdot 3H_2O$), struvite ($MgNH_4PO_4 \cdot 6H_2O$), and brushite ($CaHPO_4 \cdot 2H_2O$) ceramic scaffolds were produced via a facile 3D plotting technique combined with cementation. Light MgO was employed as the starting material, and a two-step cementation process transformed the raw material into MgPs and CaPs ceramic scaffolds. The newberyite and brushite scaffolds had good in vitro degradation and cytocompatibility, whereas the struvite scaffold caused cytotoxicity when directly combined with cells in culture, presumably due to the strong alkaline environment produced during its degradation. The experiments results showed that the 3D-plotting technique combined with subsequent cementation process could be used as a general method to fabricate CaP and MgP ceramic scaffolds. These scaffolds have the potential application in hard tissue repair.

Acknowledgements This work was supported by National Science Foundation of China (No. 21808231 and 21506236) and Science and Technology Service Network Initiative of the Chinese Academy of Sciences (No. KFJ-STZ-ZDTP-016).

Compliance with ethical standards

Conflict of interest The authors declare that they have no conflict of interest.

Publisher's note: Springer Nature remains neutral with regard to jurisdictional claims in published maps and institutional affiliations.

References

1. Wu SL, Liu XM, Yeung KWK, Liu CS, Yang XJ. Biomimetic porous scaffolds for bone tissue engineering. *Mater Sci Eng R Rep.* 2014;80:1–36.

2. Li JH, Baker BA, Mou XN, Ren N, Qiu JC, Boughton RI, et al. Biopolymer/calcium phosphate scaffolds for bone tissue engineering. *Adv Healthc Mater*. 2014;3:469–84.
3. Stevens MM. Biomaterials for bone tissue engineering. *Mater Today*. 2008;11:18–25.
4. Yu XH, Tang XY, Gohil SV, Laurencin CT. Biomaterials for bone regenerative engineering. *Adv Healthc Mater*. 2015;4:1268–85.
5. Wubneh A, Tsekoura EK, Ayranci C, Uludağ H. Current state of fabrication technologies and materials for bone tissue engineering. *Acta Biomater*. 2018;80:1–30.
6. Ma HS, Feng C, Chang J, Wu CT. 3D-printed bioceramic scaffolds: from bone tissue engineering to tumor therapy. *Acta Biomater*. 2018;79:37–59.
7. Vorndran E, Moseke C, Gbureck U. 3D printing of ceramic implants. *MRS Bull*. 2015;40:127–36.
8. Jang J, Yi HG, Cho DW. 3D printed tissue models: present and future. *ACS Biomater Sci Eng*. 2016;2:1722–31.
9. Bandyopadhyay A, Bose S, Das S. 3D printing of biomaterials. *MRS Bull*. 2015;40:108–15.
10. Kumar A, Mandal S, Barui S, Vasireddi R, Gbureck U, Gelinsky M, et al. Low temperature additive manufacturing of three dimensional scaffolds for bone-tissue engineering applications: processing related challenges and property assessment. *Mater Sci Eng R*. 2016;103:1–39.
11. Ozbolat IT, Hospodiuk M. Current advances and future perspectives in extrusion-based bioprinting. *Biomaterials*. 2016;76:321–43.
12. Lin KL, Wu CT, Chang J. Advances in synthesis of calcium phosphate crystals with controlled size and shape. *Acta Biomater*. 2014;10:4071–4102.
13. Galván-Chacón VP, Habibovic P. Deconvoluting the bioactivity of calcium phosphate-based bone graft substitutes: strategies to understand the role of individual material properties. *Adv Healthc Mater*. 2017;6:1601478.
14. Fujita H, Kudo T, Kanetaka H, Miyazaki T, Hashimoto M, Kawashita M. Adsorption of laminin on hydroxyapatite and alumina and the MC3T3-E1 cell response. *ACS Biomater Sci Eng*. 2016;2:1162–8.
15. Tamimi F, Nihouannen DL, Bassett DC, Ibasco S, Gbureck U, Knowles J, et al. Biocompatibility of magnesium phosphate minerals and their stability under physiological conditions. *Acta Biomater*. 2011;7:2678–85.
16. Ostrowski N, Roy A, Kumta PN. Magnesium phosphate cement systems for hard tissue applications: a review. *ACS Biomater Sci Eng*. 2016;2:1067–83.
17. Yu YL, Wang J, Liu CS, Zhang BW, Chen HH, Guo H, et al. Evaluation of inherent toxicology and biocompatibility of magnesium phosphate bone cement. *Colloids Surf B Biointerfaces*. 2010;76:496–504.
18. Kanter B, Geffers M, Ignatius A, Gbureck U. Control of in vivo mineral bone cement degradation. *Acta Biomater*. 2014;10:3279–87.
19. Kanter B, Vikman A, Brückner T, Schamel M, Gbureck U, Ignatius A. Bone regeneration capacity of magnesium phosphate cements in a large animal model. *Acta Biomater*. 2018;69:352–61.
20. Michna S, Wu W, Lewis JA. Concentrated hydroxyapatite inks for direct-write assembly of 3-D periodic scaffolds. *Biomaterials*. 2005;26:5632–9.
21. Franco J, Hunger P, Launey ME, Tomsia AP, Saiz E. Direct write assembly of calcium phosphate scaffolds using a water-based hydrogel. *Acta Biomater*. 2010;6:218–28.
22. Deng CJ, Yao QQ, Feng C, Li JY, Wang LM, Cheng GF, et al. 3D printing of bilineage constructive biomaterials for bone and cartilage regeneration. *Adv Funct Mater*. 2017;27:1703117.
23. Raymond S, Maazouz Y, Montufar EB, Perez RA, González B, Konkla J, et al. Accelerated hardening of nanotextured 3D-plotted self-setting calcium phosphate inks. *Acta Biomater*. 2018;75:451–62.
24. Lee J, Farag MM, Park EK, Lim J, Yun H. A simultaneous process of 3D magnesium phosphate scaffold fabrication and bioactive substance loading for hard tissue regeneration. *Mater Sci Eng C Mater Biol Appl*. 2014;36:252–60.
25. Farag MM, Yun H. Effect of gelatin addition on fabrication of magnesium phosphate-based scaffolds prepared by additive manufacturing system. *Mater Lett*. 2014;132:111–5.
26. Kim JA, Lim J, Naren R, Yun HS, Park EK. Effect of the biodegradation rate controlled by pore structures in magnesium phosphate ceramic scaffolds on bone tissue regeneration in vivo. *Acta Biomater*. 2016;44:155–67.
27. Kim JA, Yun H, Choi Y, Kim J, Choi S, Kwon T, et al. Magnesium phosphate ceramics incorporating a novel indene compound promote osteoblast differentiation in vitro and bone regeneration in vivo. *Biomaterials*. 2018;157:51–61.
28. Lai YX, Cao HJ, Wang XL, Chen SK, Zhang M, Wang N, et al. Porous composite scaffold incorporating osteogenic phyto-molecule icariin for promoting skeletal regeneration in challenging osteonecrotic bone in rabbits. *Biomaterials*. 2018;153:1–13.
29. Fischer J, Prosenic MH, Wolff M, Hort N, Willumeit R, Feyerabend F. Interference of magnesium corrosion with tetrazolium-based cytotoxicity assays. *Acta Biomater*. 2010;6:1813–23.
30. Ostrowski N, Lee B, Hong D, Enick PN, Roy A, Kumta PN. Synthesis, osteoblast, and osteoclast viability of amorphous and crystalline tri-Magnesium Phosphate. *ACS Biomater Sci Eng*. 2015;1:52–63.
31. Toshima T, Hamai R, Tafu M, Takemura Y, Fujita S, Chohji T, et al. Morphology control of brushite prepared by aqueous solution synthesis. *J Asian Ceram Soc*. 2014;2:52–6.
32. Ostrowski N, Sharma V, Roy A, Kumta PN. Systematic assessment of synthesized tri-magnesium phosphate powders (amorphous, semi-crystalline and crystalline) and cements for ceramic bone cement applications. *J Mater Sci Technol*. 2015;31:437–44.
33. Kolana K, Liu Y, Baldrige J, Murphy C, Semon J, Day D, et al. Solvent based 3D printing of biopolymer/bioactive glass composite and hydrogel for tissue engineering applications. *Procedia CIRP*. 2017;65:38–43.
34. Smith PT, Basu A, Saha A, Nelson A. Chemical modification and printability of shear-thinning hydrogel inks for direct-write 3D printing. *Polymer*. 2018;152:42–50.
35. Dai WT, Guo HL, Gao B, Ruan ML, Xu LQ, Wu JP, et al. Double network shape memory hydrogels activated by near-infrared with high mechanical toughness, nontoxicity, and 3D printability. *Chem Eng J*. 2019;356:934–49.
36. Shih KC, Shen ZQ, Li Y, Kröger M, Chang SY, Liu Y, et al. What causes the anomalous aggregation in pluronic aqueous solutions? *Soft Matter*. 2018;14:7653–63.
37. Kumar R, Kalmodia S, Nath S, Singh D, Basu B. Phase assemblage study and cytocompatibility property of heat treated potassium magnesium phosphate–silicate ceramics. *J Mater Sci Mater Med*. 2009;20:1689–95.
38. Wang AJ, Zhang J, Li JM, Ma AB, Liu LT. Effect of liquid-to-solid ratios on the properties of magnesium phosphate chemically bonded ceramics. *Mater Sci Eng C Mater Biol Appl*. 2013;33:2508–12.
39. Wang AJ, Yuan ZL, Zhang J, Liu LT, Li JM, Liu Z. Effect of raw material ratios on the compressive strength of magnesium potassium phosphate chemically bonded ceramics. *Mater Sci Eng C Mater Biol Appl*. 2013;33:5058–63.
40. Rouzic ML, Chaussadent T, Platret G, Stefan L. Mechanisms of k-struvite formation in magnesium phosphate cements. *Cem Concr Res*. 2017;91:117–22.
41. Jiang K, Zhou KG, Peng JL. Predominance diagrams for $\text{NH}_4^+ - \text{Mg}^{2+} - \text{PO}_4^{3-} - \text{H}^+ - \text{H}_2\text{O}$ system. *Chin J Inorg Chem*. 2012;28:2605–11.

42. Boistelle R, Abbona F. Morphology, habit and growth of newberyite crystals ($\text{MgHPO}_4 \cdot 3\text{H}_2\text{O}$). *J Cryst Growth*. 1981;54:275–95.
43. Sikder P, Bhaduri SB. Microwave assisted synthesis and characterization of single-phase tabular hexagonal newberyite, an important bioceramic. *J Am Ceram Soc*. 2018;101:2537–44.
44. Mehta CM, Batstone DJ. Nucleation and growth kinetics of struvite crystallization. *Water Res*. 2013;47:2890–900.
45. Muryanto S, Bayuseno AP. Influence of Cu^{2+} and Zn^{2+} as additives on crystallization kinetics and morphology of struvite. *Powder Technol*. 2014;253:602–7.
46. Bayuseno AP, Bayuseno WW. Hydrothermal synthesis of struvite and its phase transition: impacts of pH, heating and subsequent cooling methods. *J Cryst Growth*. 2018;498:336–45.
47. Dorozhkin SV, Epple M. Biological and medical significance of calcium phosphates. *Angew Chem Int Ed*. 2002;41:3130–46.
48. Soudée E, Péra J. Mechanism of setting reaction in magnesia-phosphate cements. *Cem Concr Res*. 2000;30:315–21.
49. Tan XP, Tan YJ, Chow CSL, Tor SB, Yeong WY. Metallic powder-bed based 3D printing of cellular scaffolds for orthopaedic implants: a state-of-the-art review on manufacturing, topological design, mechanical properties and biocompatibility. *Mater Sci Eng C Mater Biol Appl*. 2017;76:1328–43.
50. Wang ZW, Ma YH, Wei J, Chen X, Cao LH, Weng WZ, et al. Effects of sintering temperature on surface morphology/microstructure, in vitro degradability, mineralization and osteoblast response to magnesium phosphate as biomedical material. *Sci Rep*. 2017;7:823.
51. Mestres G, Abdolhosseini M, Bowles W, Huang SH, Aparicio C, Gorr SU, et al. Antimicrobial properties and dentin bonding strength of magnesium phosphate cements. *Acta Biomater*. 2013;9:8384–93.